CHEMISTRY
A EUROPEAN JOURNAL

DOI: 10.1002/chem.200903305

A Pre-organised Truxene Platform for Phosphorescent [Ru(bpy)$_2$] and [Os(bpy)$_2$] Metal Centres: A Clear-Cut Switch from Förster- to Dexter-Type Energy-Transfer Mechanism

Stéphane Diring,[a] Raymond Ziessel,*[a] Francesco Barigelletti,[b] Andrea Barbieri,*[b] and Barbara Ventura[b]

Abstract: We report on the synthesis, optical properties and energy-transfer features of a series of transition-metal-containing complexes and dyads, based on a pre-organised truxene scaffold. In this series, the $[Ru(bpy)_3]^{2+}$ and $[Os(bpy)_3]^{2+}$ photoactive terminals are coupled to the bridging aromatic truxene core through rigid ethynyl linkers. The photoinduced energy-transfer processes taking place from the Ru- to the Os-based levels, and from the truxene bridging ligand to the terminal-metal chromophores are studied and the pathways and mechanisms are discussed. The photoinduced energy-transfer process observed in the dyad proceeds rapidly through: i) an efficient $^1L \rightarrow {}^1Os$ direct energy transfer followed by intersystem crossing to ^3Os, and ii) a fast $^1L \rightarrow {}^1Ru$ energy-transfer step and subsequent intersystem crossing to ^3Ru followed by a $^3Ru \rightarrow {}^3Os$ energy-transfer process. The first $^1L \rightarrow {}^1Os$ and $^1L \rightarrow {}^1Ru$ steps are controlled by a dipole–dipole interaction (Förster mechanism), whereas the subsequent $^3Ru \rightarrow {}^3Os$ step proceeds by means of a long-range ($\approx$24 Å) through-bond mediated Dexter mechanism, facilitated by the conjugation along the bpy-truxene-bpy molecular axis.

Keywords: bipyridine · energy transfer · osmium · photophysics · ruthenium · truxene

Introduction

An important thrust of current work is to gather luminophores with large absorption cross-sections into pre-organised architectures.[1,2] Truxene (10,15-dihydro-5*H*-diindeno[1,2-α;1′,2′-*c*]fluorene) is a C_3-symmetrical scaffold in which the three peripheral phenylene rings are all *meta*-substituted to the central phenyl ring.[3] Not surprisingly, the truxene π system has properties similar to the fluorene π system, which has been proven to be a suitable building block for chromophores and transition metals.[4] Unlike fluorene, which can only be used for building one-dimensional chromophores, truxene can readily be functionalised in three directions in space to serve as an excellent building block for larger and dendritic structures. During the past decades truxene has been used as a potential starting material for the construction of liquid-crystalline compounds,[5,6] bowl-shaped fragments of fullerenes[7] and C_3-tripodal materials for chiral recognition.[8] Recently synthesised truxene derivatives include a variety of star-shaped oligomers and dendritic structures with extended π conjugation[9] of the polyaromatic core, as well as truxene-based donor–acceptor systems for use as multifunctional fluorescent probes.[10] Truxene has scarcely been associated with N-heterocyclic derivatives, but there is only one case in which three π-conjugated terpyridine ligands have been linked to truxene in a symmetric fashion leading to blue emission in solution.[11] In one case truxene has been covalently linked to phosphorescent platinum(II) metal centres.[12] The challenge here is to present synthetic strategies allowing to link different mod-

[a] Dr. S. Diring, Prof. R. Ziessel
Laboratoire de Chimie Organique et Spectroscopies Avancées (LCOSA)
Ecole de Chimie, Polymères, Matériaux (ECPM)
Université de Strasbourg (UdS), 25 rue Becquerel
67087 Strasbourg Cedex 02 (France)
Fax: (+33) 0368-85-2761
E-mail: ziessel@unistra.fr
Homepage: http://www-lmspc.u-strasbg.fr/lcosa

[b] Dr. F. Barigelletti, Dr. A. Barbieri, Dr. B. Ventura
Istituto per la Sintesi Organica e la Fotoreattività (ISOF)
Consiglio Nazionale delle Ricerche (CNR)
Via P. Gobetti 101, 40129 Bologna (Italy)
Fax: (+39) 051-639-9844
E-mail: andrea.barbieri@isof.cnr.it

Supporting information for this article is available on the WWW under http://dx.doi.org/10.1002/chem.201000211.

ules to a truxene platform, in a synthetically controlled fashion.

The study of photoinduced energy-transfer processes in supramolecular multichromophoric arrays containing photoactive subunits has been extensively pursued because these systems represent useful models for the understanding of naturally occurring processes in photosynthesis and have potential applications in artificial light-driven photochemical molecular machines and in optoelectronic devices.[13–18]

In this paper we report on the synthesis, optical properties and energy-transfer features of a series of transition metal-containing complexes and dyads, based on a truxene core, schematically illustrated in Scheme 1. In this series, the Ru– and Os–polypyridine photoactive terminals are coupled to the bridging aromatic truxene scaffold through rigid ethynyl linkers.

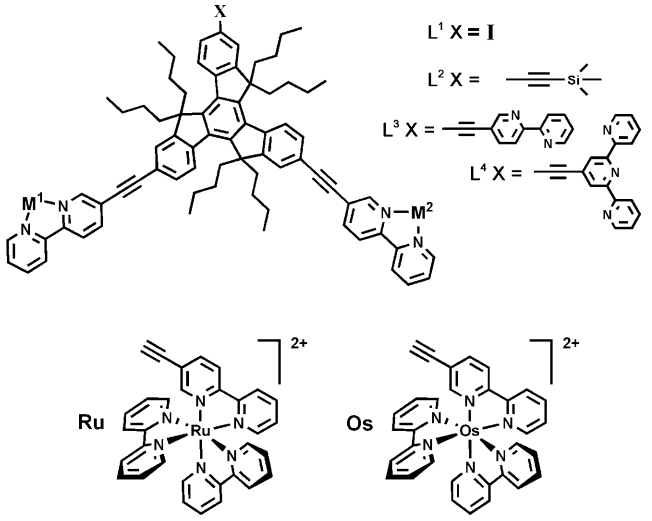

Scheme 1. Schematic structure of ligand and complexes. Bpy: 2,2′-bipyridine; ≡–bpy: 5-ethynyl-2,2′-bipyridine; ≡–tpy:4′-ethynyl-2,2′:6′,2″-terpyridine.

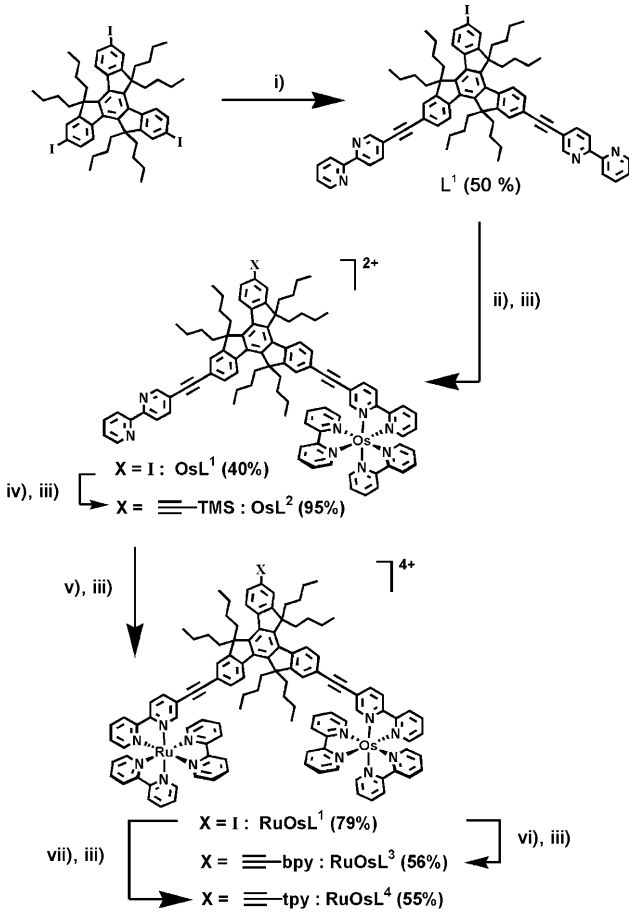

Scheme 2. i) 5-Ethynyl-2,2′-bipyridine (2 equiv), $[Pd(PPh_3)_4]$ (12%), *n*-propylamine, 60°C, 18 h; ii) $[Os(bpy)_2Cl_2]$ (1 equiv), EtOH, microwave 1200 W, 180°C, 1 h; iii) KPF_6, DMF, H_2O; iv) trimethylsilylacetylene, $[Pd(PPh_3)_4]$ (12%), diisopropylamine, acetonitrile, 65°C, 18 h; v) $[Ru(bpy)_2Cl_2]$, EtOH, CH_2Cl_2, 80°C, 72 h; vi) 5-ethynyl-2,2′-bipyridine, $[Pd(PPh_3)_4]$ (14%), DMF, diisopropylamine, 75°C, 18 h; vii) 4′-ethynyl-2,2′:6′,2”-terpyridine, $[Pd(PPh_3)_4]$ (14%), DMF, diisopropylamine, 75°C, 18 h.

Results and Discussion

Synthesis: The ligand $\mathbf{L^1}$ was obtained by reacting 2,7,12-triiodo-5,5′,10,10′,15,15′-hexabutyltruxene with two equivalents of 5-ethynyl-2,2′-bipyridine through a palladium(0) promoted statistical cross-coupling reaction (Scheme 2). The di-substituted compound could be easily isolated from mono and tri-substituted side products by aluminium-oxide chromatography followed by recrystallisation in appropriate solvent mixtures. Further complexation reactions with one equivalent of ruthenium(II) or osmium(II) $[M^{II}(bpy)_2Cl_2]$ complexes afforded $\mathbf{RuL^1}$ and $\mathbf{OsL^1}$, respectively. Considering the difficulty of complexing the osmium(II) cation,[19] we performed the reaction by microwave assisted heating. After only one hour at 180°C, $\mathbf{OsL^1}$ could be isolated in reasonable yield (40%). In the case of ruthenium(II), classical reflux in ethanol for 72 h gave $\mathbf{RuL^1}$ in 50% isolated yield. Systematic counter-ion exchange with KPF_6 salt was accomplished to enhance the solubility of the complexes in organic media. The acetylenic functionality in $\mathbf{OsL^2}$ was introduced almost quantitatively by means of a Sonogashira cross-coupling reaction with trimethylsilylacetylene. Refluxing $\mathbf{OsL^1}$ with $[Ru(bpy)_2Cl_2]$ in ethanol allowed the complexation of the remaining bipyridine fragment to afford the bimetallic complex $\mathbf{RuOsL^1}$ in 79% yield. Finally, additional pendent chelating fragments, that is, 2,2′-bipyridine and 2,2′:6′,2″-terpyridine to complex $\mathbf{RuOsL^1}$ could be easily connected by ethynyl linkers by means of palladium(0) promoted cross-coupling reactions to afford $\mathbf{RuOsL^3}$ and $\mathbf{RuOsL^4}$, respectively.

It is worth noting that the present ligand and complexes represent the first examples of non-symmetrical substituted truxene molecules grafted by a variety of three different modules, each of them being prepared in a controlled manner.

All compounds were unambiguously characterised by using ^{1}H NMR spectroscopy, mass spectrometry and elemental analysis. The solubility gained from the six butyl chains grafted on the truxene core, as well as the hexafluorophosphate counter ions, enabled us to record well defined ^{1}H NMR spectra, even for the bimetallic complexes (Figure 1). All signals for **L^1** were carefully assigned (and confirmed by 2D COSY experiments). As is usually observed for pyridine derivatives, the most deshielded signals, a and d ($\delta = 8.89$ and 8.72 ppm, respectively), refer to the protons in the *ortho* position of the nitrogen atom, whereas the most shielded signal e ($\delta = 7.45$ ppm) corresponds to the protons in the *meta* position. Protons H_{T4} and $H_{T4''}$ on the aromatic truxene core have a similar electromagnetic environment and are represented by a doublet at $\delta = 8.56$ ppm, whereas proton $H_{T4'}$ (on the phenyl ring bearing the iodine atom) yields a doublet at $\delta = 8.36$ ppm. Upon coordination of one osmium(II) cation (**OsL^1**), the aromatic pattern becomes more complex, owing to additional bipyridine fragments and loss of symmetry. In addition to the expected integration value of aromatic protons, the signal d at $\delta =$ 8.72 ppm (remains unchanged with respect to **L^1**) confirms the presence of an uncomplexed bipyridine fragment. Interestingly, proton $H_{T4'}$ give rise to two doublets with an integration ratio of 1-to-1. **OsL^1** consists of three different fragments ("Os", "bpy" and "I") connected to the truxene aromatic periphery and exists as a mixture of two regioisomers (see structure in the Supporting Information). The signal $H_{T4'}$ reflects the existence of these two regioisomers in a 1-to-1 ratio. Finally, the complexation of the remaining bipyridine fragment in **OsL^1** by the ruthenium(II) cation leading to **RuOsL^1** is reflected by the unambiguous disappearance of signals d, b and g, as well as an increased value for the integration of protons. It can be noted that protons H_{T4} and $H_{T4''}$ give rise to a single doublet ($\delta =$ 8.53 ppm), indicating that the octahedral ruthenium(II) and osmium(II) fragments are producing very close electromagnetic environments.

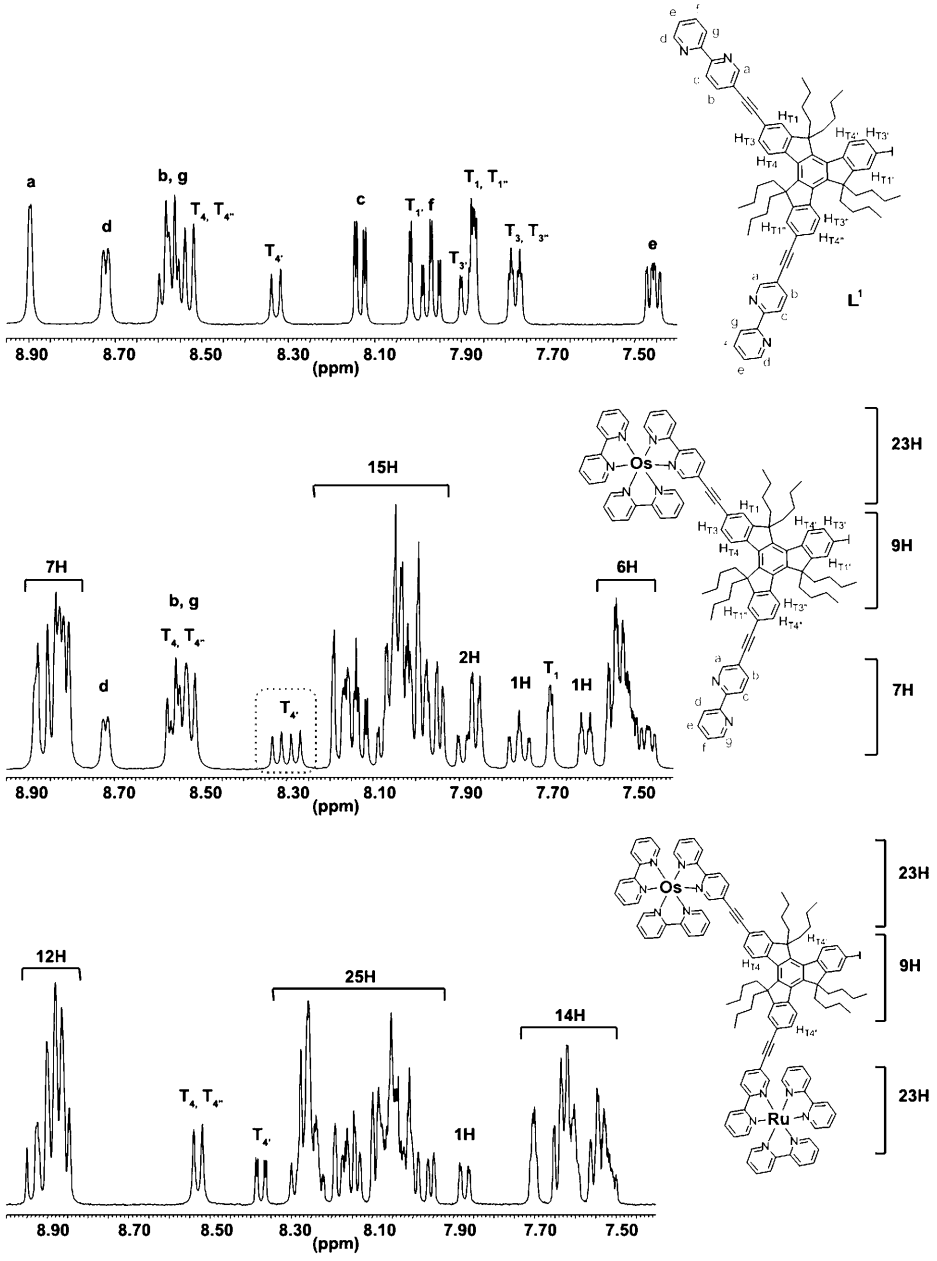

Figure 1. ^{1}H NMR spectra of compounds **L^1**, **OsL^1** and **RuOsL^1** in $(CD_3)_2CO$, 400 MHz; for the sake of clarity only the aromatic regions are represented).

Absorption: The absorption spectra of the mononuclear complexes **RuL^1**, **OsL^1** and **OsL^2** in ACN and that of the truxene ligand **L^1** in DCM are compared in Figure 2, whereas the spectra of the dyads **RuOsL^1**, **RuOsL^3** and **RuOsL^4** are collected in Figure 3. Concerned absorption data are listed in Table 1. The truxene bridging ligand **L^1** shows an envelope of absorption bands localised in the spectral region between $\lambda = 250$ and 400 nm (Figure 2), with maxima at $\lambda =$ 352 and 373 nm ($\varepsilon = 104\,900$ and $95\,300\,M^{-1}cm^{-1}$, respectively). The absorption bands are attributed to $^1\pi,\pi^*$ transitions of the truxene aromatic core, red-

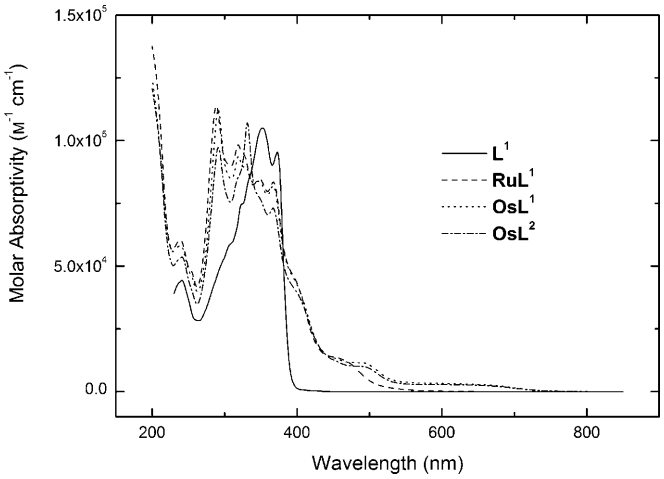

Figure 2. Ground state absorption spectra in air-equilibrated solvents of ligand **L^1** in dichloromethane (——) and mononuclear complexes **RuL^1** (-----), **OsL^1** (•••••) and **OsL^2** (–•–•) in acetonitrile.

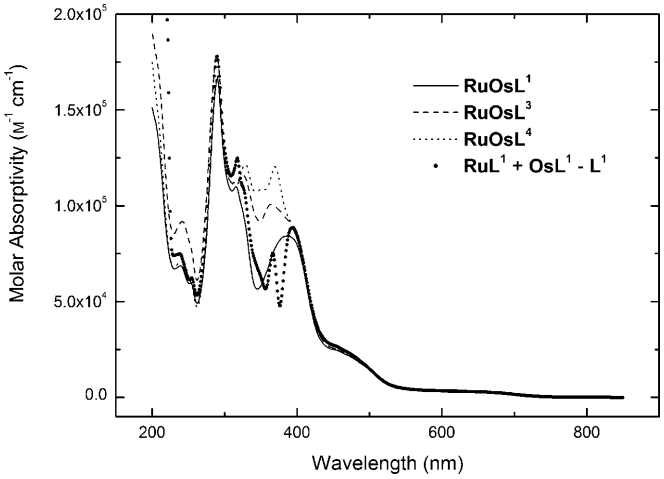

Figure 3. Ground state absorption spectra of dyads **RuOsL^1** (——), **RuOsL^3** (-----) and **RuOsL^4** (•••••) in air-equilibrated acetonitrile. Spectral addition of **RuL^1** and **OsL^1** absorption subtracted by the **L^1** contribution is also shown (●).

Table 1. Absorption properties of ligand **L^1**, complexes and dyads.[a]

	λ_{max} [nm (ε_{max}, M^{-1}cm^{-1})]
L^1	240 (44,200); 352 (104,900); 373 (95,300)
RuL^1	239 (60,500); 288 (113,700); 319 (98,300); 348 (84,700); 367 (83,600); 450 (13,800)
OsL^1	238 (58,200); 291(112,500); 319 (93,800); 347 (83,800); 367 (82,100); 480 (11,600); 600 (3,300)
OsL^2	241 (53,600); 291 (97,300); 331(107,100); 367 (73,100); 480 (10,100); 600 (2,800)
RuOsL^1	239 (68,700); 290 (166,600); 316 (110,000); 386 (84,300); 470 (22,000); 600 (3,300)
RuOsL^3	242 (91,800); 289 (178,300); 326 (115,900); 364 (100,600); 470 (22,100); 600 (3,500)
RuOsL^4	241 (72,300); 290 (167,900); 329 (121,600); 369 (120,400); 470 (22,200); 600 (3,300)

[a] In air-equilibrated solvents, CH_2Cl_2 for **L^1** and CH_3CN for the complexes, at 298 K.

shifted with respect to those of neat truxene,[20] owing to the increased conjugation brought by the acetylene linked bipyridine groups, in analogy with observations of other conjugated truxene derivatives.[9,21,22] The mononuclear Ru^{II} complex **RuL^1** and the two Os^{II} complexes **OsL^1** and **OsL^2**, in addition to the absorption bands of the truxene core, display intense and narrow bands localised in the UV region (λ_{max} = 290 nm, ε in the order of 110000 M^{-1}cm^{-1}), typical of the $^1\pi,\pi^*$ bpy-centered transitions, and broad ^{1}MLCT transitions in the visible,[23,24] that maximise at $\lambda = 450$ and 480 nm (with $\varepsilon = 10000$–13000 M^{-1}cm^{-1}) for **RuL^1** and Os complexes, respectively. For the Os-containing complexes **OsL^1** and **OsL^2** an additional absorption tail peaking at $\lambda \approx 600$ nm ($\varepsilon \approx 3000$ M^{-1}cm^{-1}) is also registered, owing to formally forbidden Os-based direct absorption from the ground state to the ^{3}MLCT level,[24] induced by the strong spin-orbit coupling of the Os^{II} centre ($\zeta_{Os} = 3381$ cm^{-1}).[25] The absorption spectral features of the three **RuOsL^n** dyads ($n = 1$, 3 and 4) are interpreted in terms of the individual electronic properties of the components discussed above. Thus, the contribution from i) the bpy-centred $^1\pi,\pi^*$ absorption at $\lambda = 290$ nm, ii) the truxene-centred $^1\pi,\pi^*$ absorption between $\lambda = 300$ and 400 nm, partially overlapping with iii) the ^{1}MLCT band from the Ru→bpy and Os→bpy transitions, and iv) the low energy band typical of the ^{3}MLCT Os-based direct absorption can be easily singled out. The 1.5 time increase and the doubling of the epsilon values of the bpy-centred and M→bpy transitions at $\lambda = 290$ and 450–480 nm, respectively, observed in the dyads with respect to the mononuclear complexes is clearly attributable to the presence of a larger number of coordinated bpy units in the former case. The spectrum of the dyad **RuOsL^1** matches reasonably well the superposition of the spectra of the single components **RuL^1** and **OsL^1**, provided the contribution of the ligand **L^1** is subtracted from the sum (Figure 3), thus, indicating a weak interaction between the Ru-bpy and Os-bpy satellite chromophores. The differences showed by **RuOsL^3** and **RuOsL^4** in the spectral region $\lambda = 350$–400 nm with respect to the features displayed by the **RuOsL^1** complex have to be ascribed to the presence of different terminal groups linked to truxene (X substituent in Scheme 1) in the three dyads, influencing to a different extent the electronic transitions originating from the truxene core.

Emission: The room temperature luminescence profiles of the ligand in DCM and of the examined complexes in ACN air-free solutions are reported in Figure 4, and the relevant photophysical data are collected in Table 2. Ligand **L^1** shows an intense emission at $\lambda = 408$ nm in DCM with $\phi_{em} = 0.70$ and a lifetime $\tau = 0.86$ ns. (Table 2). The emission is red-shifted with respect to that of simple truxene that occurs in the range $\lambda = 350$–400 nm,[9,20–22] and this shift can be safely attributed to the presence of bipyridine groups linked to the truxene core by acetylene linkers that increase the electronic delocalisation, an effect already observed for conjugated truxene dimers.[22] The lifetime of **L^1** is of the same order of magnitude of values reported for halogen-containing trux-

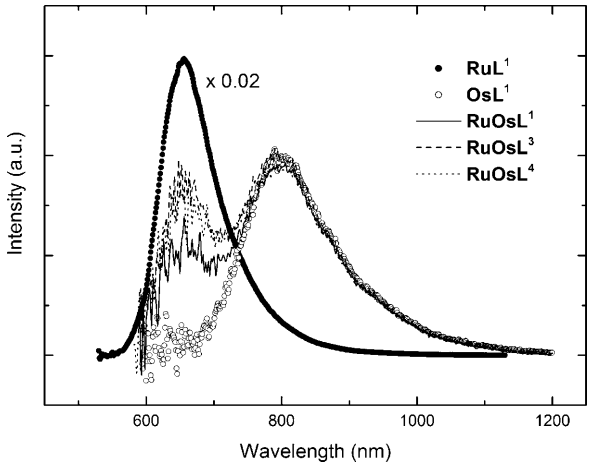

Figure 4. Room-temperature corrected emission spectra of isoabsorbing solutions at 470 nm of **RuL¹** (●), **OsL¹** (○), **RuOsL¹** (——), **RuOsL³** (-----) and **RuOsL⁴** (·····) in air-free acetonitrile solutions. Excitation at $\nu = 470$ nm. Spectral area proportional to the emission quantum yield. The emission spectrum of **RuL¹** is divided by 50.

Table 2. Luminescence data for ligand **L¹**, mononuclear complexes and dyads.[a]

	298 K			77 K		
	λ_{max}[b] [nm]	ϕ[c]	τ[d] [s]	λ_{max}[b] [nm]	τ[d] [μs]	E [eV]
L¹	408	7.0×10^{-1}	0.86×10^{-9}	382, 404	0.71×10^{-3}	3.25
Ru[e]	652	5.4×10^{-2}	0.80×10^{-6}	619	4.6	2.02
RuL¹	655	7.3×10^{-2}	1.04×10^{-6}	614	4.5	2.02
Os[e]	798	7.6×10^{-4}	16.0×10^{-9}	736	2.3	1.68
OsL¹	801	1.1×10^{-3}	22.2×10^{-9}	744	0.84	1.67
OsL²	802	1.1×10^{-3}	18.1×10^{-9}	742	0.75	1.67
RuOsL¹	655	5.9×10^{-4}[f]	2.30×10^{-9} -2.5×10^{-9}[g]	616	n.d.	2.01
	805	1.0×10^{-3}	22.6×10^{-9}	746	0.82	1.66
RuOsL³	655	8.3×10^{-4}[f]	2.30×10^{-9} _[g]	618	n.d.	2.01
	805	1.1×10^{-3}	22.7×10^{-9}	742	0.66	1.67
RuOsL⁴	655	8.0×10^{-4}[f]	2.50×10^{-9} _[g]	618	n.d.	2.01
	806	1.0×10^{-3}	22.6×10^{-9}	746	0.78	1.66

[a] In oxygen-free solvents, CH_2Cl_2 for **L¹** and CH_3CN for the complexes, at 298 K. In MeOH/EtOH (1:4 v/v) at 77 K. [b] From corrected emission spectra. [c] $\lambda_{exc} = 350$ nm for **L¹**, $\lambda = 470$ nm for Ru-based emission and $\lambda = 600$ nm for Os-based emission. [d] $\lambda_{exc} = 331$ nm for **L¹**, $\lambda = 465$ nm for Ru-based emission and $\lambda = 560$ nm for Os-based emission. [e] From Ref. [19] partially revised. [f] Ru-based emission quantum yield calculated with respect to **RuL¹** emission at $\lambda = 655$ nm. [g] Rise time of the Os luminescence; for **RuOsL³** and **RuOsL⁴** it was not possible to fit the rise.

enes,[26,27] but notably the emission quantum yield is unusually high and this results in a high k_r value of 8×10^8 s^{-1}. The Ru and Os complexes (**RuL¹**, **OsL¹** and **OsL²**) display luminescence properties (Table 2) similar to those previously observed[19] for their precursors **Ru** and **Os** (Scheme 1), here reported as sake of comparison. Notably, the truxene-containing complexes display an emission quantum yield about 40% higher than the respective precursors **Ru** and **Os**. The lower lifetime at 77 K of the Os complexes **OsL¹** and **OsL²** (700–800 ns) with respect to that of **Os** (2.3 μs) is in analogy with data reported for polypyridyl-based Os complexes for which one ligand is a polyaromatic group.[28]

From inspection of Figures 2 and 3 it emerges that selective excitation of the Os fragment in the dyads is achievable at $\lambda > 550$ nm, whereas excitation at $\lambda = 470$ nm produces a 1:1 proportion of ^{3}MLCT excited states localised on Ru and Os. The room temperature emission spectra registered upon selective excitation of the Os complexes in models **OsL¹** and **OsL²** and in the three dyads **RuOsL¹**, **RuOsL³** and **RuOsL⁴**, present very similar features: the emission quantum yield is around 1.0×10^{-3} and the lifetime approximately 20 ns in all cases (Table 2), indicating that there is not a strong perturbation of the electronic properties of the Os(bpy)$_2$–truxene type complex if it is inserted in the different arrays, as already evidenced from the addition of the absorption spectra of the components (Figure 3). The lifetimes at 77 K of the Os-based emission of the three dyads are in the same range of those of models **OsL¹** and **OsL²** (Table 2).

Emission spectra registered at room temperature upon excitation at $\lambda = 470$ nm of isoabsorbing acetonitrile solutions of the three dyads and models **RuL¹** and **OsL¹** are shown in Figure 4, and the related data are reported in Table 2 (the emission spectrum of model **OsL²** is not reported in the figure, as it is very similar to that of **OsL¹**, see Table 2). The luminescence of the Ru unit is reduced to about 1% that of model **RuL¹** in all the three dyads **RuOsL¹**, **RuOsL³** and **RuOsL⁴**, whereas the yield of the Os-based ^{3}MLCT emission is almost identical to that of model **OsL¹** in all cases (Figure 4 and Table 2). The residual emission of the Ru unit in the three dyads has a lifetimes of approximately 2.5 ns, whereas the lifetime of the unquenched **RuL¹** is 1040 ns. A rise in the Os luminescence upon excitation at $\lambda = 470$ nm is observed in all dyads, and in the case of **RuOsL¹** a value of 2.5 ns for the rise could be estimated (Table 2), coincident with the quenched lifetime of the Ru-based emission. These results point to the presence of a very efficient energy-transfer process from the Ru unit to the Os unit in all the examined dyads. A similar behaviour is observed at low temperature in a glassy matrix; comparing the emission spectra of isoabsorbing MeOH/EtOH (1:4 v/v) solutions of the three dyads and models **RuL¹** and **OsL¹** excited at $\lambda = 470$ nm, in fact, an evident quenching of the Ru-based emission and an almost complete recovering of the Os-based luminescence are observed in all dyads (Figure 5).

Energy transfer: According to a simplified view, the Ru and Os components in the dyad could be regarded to a certain extent as electronically isolated. Actually, the absorption profiles of the **RuOsL¹** complex satisfactorily corresponds to

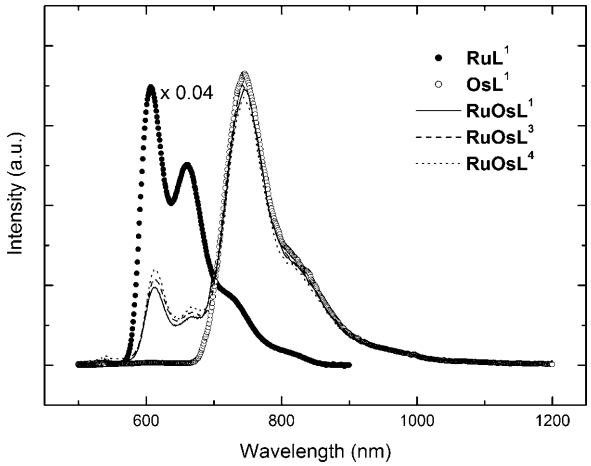

Figure 5. Corrected emission spectra of isoabsorbing solutions at $\lambda=$ 470 nm of **RuL^1** (●), **OsL^1** (○), **RuOsL^1** (——), **RuOsL^3** (-----) and **RuOsL^4** (·····) at 77 K in MeOH/EtOH (1:4 v/v) glassy solutions. Excitation at $\lambda=470$ nm. The emission spectrum of **RuL^1** is divided by 25.

the sum of the spectra of the component mononuclear complexes **RuL^1** and **OsL^1** (Figure 3). In addition, the low energy portion of the luminescence profile of the dinuclear complexes **RuOsL^n** ($n=1$, 3, 4) quite nicely overlaps with the emission profile of **OsL^1** (Figures 4 and 5), another indication supporting the model based on isolated components. The extent of the electronic isolation drawn from spectroscopic measurements does not mean that there is no electronic interaction at all between the various components, rather, this interaction is sufficiently weak not to significantly affect the band maxima and profiles (both for absorption and emission) in the multi-component species.

Based on the assumption of electronically isolated components in the multinuclear arrays studied it is possible to draw the excited states energy layout for these species. Such an energy level diagram for **RuOsL^1** is shown in Figure 6, as obtained by estimating the various levels from the band maxima of the 77 K luminescence spectra of the components

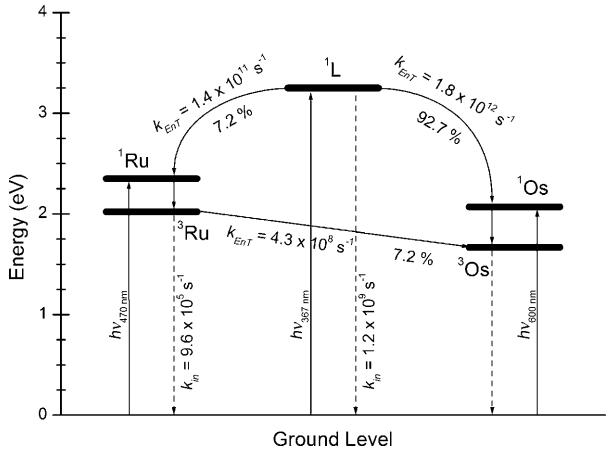

Figure 6. Energy levels (in eV) of selected excited states and photoinduced energy-transfer processes in the examined complexes.

by using the results from complexes **RuL^1** and **OsL^1** and from ligand **L^1**. Metal-based singlet levels have been estimated on the basis of the onset of the lowest energy-absorption band of **RuL^1** and **OsL^1**, for ^{1}Ru and ^{1}Os, respectively. From inspection of the energy-level plot it appears that ligand **L^1** has an energy content higher than that of both Ru- and Os- based units in dyads **RuOsL^1**, **RuOsL^3** and **RuOsL^4**; its singlet excited state, lies at 3.25 eV, see Table 2. The energy-transfer processes from ^{1}L to Ru and Os units are, therefore, both possible, as depicted in Figure 6; the processes $^1L\rightarrow{}^1Ru$ and $^1L\rightarrow{}^1Os$ are exoergonic by approximately 0.9 and 1.2 eV, respectively. To assess if these photoinduced processes take place, we considered the complexes **RuL^1** and **OsL^1** as models for the absorption features of the dyad **RuOsL^1**. A comparison between the absorption spectra of **L^1**, **RuL^1** and **OsL^1** leads us to identify three different excitation wavelengths yielding distinct excited-state levels, namely: i) at $\lambda=367$ nm, for which about 95% in **RuL^1**, and 85% in **OsL^1**, of the photons are absorbed by the truxene ligand **L^1** (Figure 2); ii) at $\lambda=470$ nm, for which roughly a 1:1 ratio in the Ru- and Os-based levels in the dyad is expected from comparison of **RuL^1** and **OsL^1** absorption curves ($\varepsilon_{470}=11\,800$ and $11\,700\,M^{-1}cm^{-1}$, respectively), whereas pure Ru-based emission can be obtained from **RuL^1**; iii) at $\lambda=600$ nm, for which pure Os-based emission from **OsL^1** and **OsL^2** is observed upon selective excitation.

The luminescence of isoabsorbing solutions at $\lambda=367$ nm of **L^1**, **RuL^1**, **OsL^1** and dyad **RuOsL^1** is reported in Figure 7 and compared to the emission spectra of **RuL^1** excited at $\lambda=470$ nm, and **OsL^1** excited at $\lambda=600$ nm, used as a single metal-based emission reference, the spectral area being proportional to the emission quantum yield (see Table 2). The spectra of **OsL^2** and dyads **RuOsL^3** and **RuOsL^4** are not re-

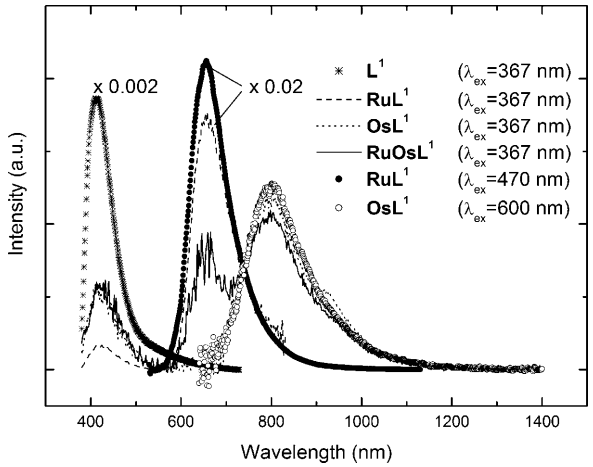

Figure 7. Corrected emission spectra in air-free solutions of **L** (*) in dichloromethane, and of **RuL^1** (-----), **OsL^1** (·····) and, **RuOsL^1** (——) excited at $\lambda=367$ nm in acetonitrile solutions. Emission spectra of **RuL^1** excited at $\lambda=470$ nm (●) and of **OsL^1** excited at $\lambda=600$ nm (○) are reported as reference. All spectral areas are proportional to the photoluminescence quantum yield. The spectrum of **L^1** is divided by 500, whereas those of **RuL^1**, obtained upon excitation at $\lambda=367$ and 470 nm, are both divided by 50.

ported as they are very similar to those of **OsL^1** and **RuOsL^1**, respectively. From inspection of Figure 7 it emerges that upon excitation at $\lambda = 367$ nm of the complexes **RuL^1** (Figure 7, -----) and **OsL^1** (Figure 7, •••••) the fluorescence of ligand **L^1** at $\lambda = 408$ nm is almost completely quenched, whereas the Ru-based and the Os-based emissions are almost completely recovered. On the other hand, the quenching of the truxene ligand luminescence in the dyad **RuOsL^1** (Figure 7, ——) is accompanied by the quenching of the Ru-based emission and a substantial recovery of the Os luminescence, as indicated by the quantum yields listed in Table 2.

As already observed, upon excitation of the Ru^{II} chromophore at $\lambda = 470$ nm, in the three dyads **RuOsL^1**, **RuOsL^3** and **RuOsL^4** a residual Ru-based luminescence is observed at room temperature ($\phi_{Ru} = 5.9 \times 10^{-4}$, $\tau = 2.30$ ns, Table 2) and in frozen solution at 77 K (Figure 5), beside an almost complete recovery of the Os-based emission ($\phi_{Os} = 1.0 \times 10^{-3}$, $\tau = 22.6$ ns, Table 2). Moreover, for the latter, a rise time $\tau = -2.5$ ns which closely matches the residual lifetime emission from the Ru-based levels has been observed.

The obtained results can be explained either i) by a direct $^1L \rightarrow {}^1Os$ energy transfer followed by ultrafast intersystem crossing to ^3Os or ii) by a first $^1L \rightarrow {}^1Ru$ energy-transfer step and subsequent intersystem crossing to ^3Ru followed by a $^3Ru \rightarrow {}^3Os$ energy-transfer process (see Figure 6). For the direct $^1L \rightarrow {}^1Os$ energy transfer we find, by using Equation (4) in the Experimental Section, a very fast $k_{EnT} = 1.8 \times 10^{12}\ s^{-1}$ and an efficiency $\eta_{EnT} = 0.927$ (Figure 6), whereas the $^1L \rightarrow {}^1Ru$ process takes place with a rate constant one order of magnitude lower ($k_{EnT} = 1.4 \times 10^{11}\ s^{-1}$, $\eta_{EnT} = 0.072$). Then, by using Equation (3) (see the Experimental Section), the rate constant k_{EnT} values obtained for the $^3Ru \rightarrow {}^3Os$ process are $4.3 \times 10^8\ s^{-1}$, $4.3 \times 10^8\ s^{-1}$ and $4.0 \times 10^8\ s^{-1}$ for **RuOsL^1**, **RuOsL^3**, and **RuOsL^4**, respectively, whereas the corresponding efficiency η_{EnT} calculated from Equation (5) (see the Experimental Section) is 99.8%. Therefore, upon excitation of the ligand-based energy levels most of the energy is rapidly transferred to the osmium centre, while the remaining portion is first put on the Ru-based levels and subsequently almost completely drained to the low-lying excited-state levels of the [Os(bpy)$_2$] moiety. As a final result, almost all of the energy placed on the different components of the multinuclear array is very efficiently (total $\eta_{EnT} = 0.9988$) and rapidly transferred to the Os centre, which acts as the final energy collector. The likely energy-transfer mechanism is discussed in detail below.

For cases of weakly interacting partners several approaches are available to determine the type of energy transfer, and expressions for rate constants can be derived from application of the Fermi's Second Golden Rule, Equation (1),[29]

$$k = \frac{4\pi^2}{h} H^2 FC \qquad (1)$$

in which H^2 is the electronic interaction term between the initial and final states and *FC* is the Franck–Condon factor describing the overlap between the donor and acceptor vibrational modes that are coupled to the energy-transfer process. To describe the energy-transfer steps within multimetal assemblies, two limit mechanisms can be invoked: i) in one case the intermetal interaction is viewed to take place by means of dipole–dipole through-space interactions (Förster mechanism, *F*),[30] ii) on the other hand, in the presence of suitable bridging ligands allowing for a small, but effective, electronic communication, a through-bond double-electron exchange (Dexter mechanism, *D*)[31] might be appropriate to account for such interactions.

Use of available spectroscopic properties, the emission spectrum of the donor models (**L^1** and **RuL^1**) and the absorption spectrum of the acceptor models (**RuL^1** and **OsL^1**) allows us to calculate for the dyad **RuOsL^1** the spectral overlap J_F and J_D, and, for the case of the Förster mechanism, the critical radius, R_c, defined as the interchromophoric distance at which k_F equals k_{in} (see the Experimental Section). In Table 3 the main parameters used to evaluate the energy-transfer features in the **RuOsL^1** dyad are summarised.

Table 3. Parameters used to evaluate the features of the energy-transfer processes within the **RuOsL^1** dyad.

	k_{EnT} [s^{-1}][a]	J_F [$cm^3\,M^{-1}$]	R_c [Å]	d [Å][b]	J_D [cm]	H [cm^{-1}][c]
$^1L \rightarrow {}^1Os$	1.8×10^{12}	7.8×10^{-14}	46.2	13.6	1.4×10^{-4}	105.6
$^1L \rightarrow {}^1Ru$	1.4×10^{11}	7.2×10^{-14}	45.6	20.6	1.5×10^{-4}	27.69
$^3Ru \rightarrow {}^3Os$	4.3×10^8	3.7×10^{-14}	28.0	10.1	1.8×10^{-4}	1.44

[a] Experimental energy-transfer-rate constant calculated from Equations (3) and (4). [b] Interchromophoric distance calculated for $k_F = k_{EnT}$. [c] Electronic interaction factor calculated for $k_D = k_{EnT}$.

With regard to the Förster-type mechanism in the case of the $^1L \rightarrow {}^1Os$ energy-transfer process, the spectral overlap between the luminescence profile of **L^1** and the absorption profile of **OsL^1** affords an overlap integral $J_F = 7.8 \times 10^{-14}\ cm^3 M^{-1}$ and a critical radius $R_c = 46.2$ Å, while for the $^1L \rightarrow {}^1Ru$ energy-transfer step similar values for $J_F = 7.2 \times 10^{-14}\ cm^3 M^{-1}$ and $R_c = 45.6$ Å have been calculated (Table 3). According to the obtained J_F value a distribution of energy-transfer-rate constants k_F can be calculated as function of the interchromophoric distance d (see the Experimental Section). Under full control of the energy-transfer process by the dipole–dipole interaction mechanism, a distance $d = 13.6$ Å is obtained to account for the observed experimental rate-constant value, that is, in the case of $k_F = k_{EnT}$. For the $^1L \rightarrow {}^1Ru$ energy-transfer step a larger distance $d = 20.6$ Å is obtained for $k_F = 1.4 \times 10^{11}\ s^{-1}$, using the calculated $J_F = 7.2 \times 10^{-14}\ cm^3\,M^{-1}$ and $R_c = 45.6$ Å (Table 3). These distances are comparable to the truxene donor-metal acceptor separation that could be assumed on the basis of the molecular modelling of the **RuL^{1}Os** complex as represented in Figure 8. In fact, a certain conformational freedom is possible for the rotation of the pendant metal bipyridyl chromo-

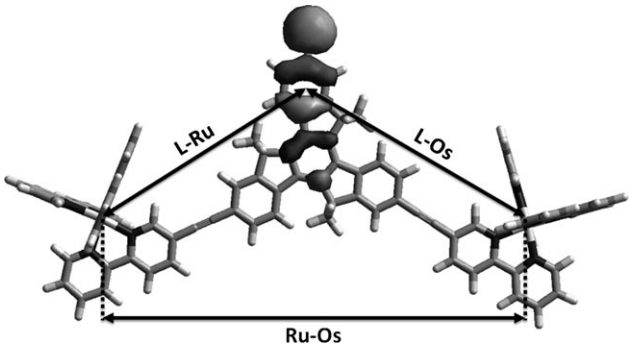

Figure 8. HOMO distribution in the complex **RuOsL^1** obtained for a minimum-energy geometry calculated by PM6 semiempirical method. The relevant truxene-metal and intermetal distances are: d(L-Ru) = 15.6 ÷ 16.7 Å, d(L-Os) = 14.1 ÷ 16.1 Å and d(Ru-Os) = 21.9 ÷ 25.3 Å, depending on the molecular configuration.

phores around the triple bond of the truxene side arms. In this case, four conformations of similar minimum energy (two *transoid* and two *cisoid*) have been identified and a distribution of distances between the centre of the HOMO, located on the truxene core according to semiempirical PM6 calculation, and the Ru^{II} and Os^{II} metals, d(L-Os) = 14.1 ÷ 15.1 Å and d(L-Ru) = 15.6 ÷ 16.7 Å, has been calculated (Figure 8).[32] By introducing these values together with the other parameters into Equation (6) (see the Experimental Section), two sets of rate constants $k_F = 0.9 \div 1.4 \times 10^{12}\ s^{-1}$ and $k_F = 4.8 \div 7.2 \times 10^{11}\ s^{-1}$ for the $^1L \rightarrow {}^1Os$ and $^1L \rightarrow {}^1Ru$ energy-transfer steps, respectively, are derived. In the case of the double-electron-exchange model, on the basis of the calculated overlap integrals J_D, for the Dexter-type mechanism to take control over the $^1L \rightarrow {}^1Os$ and $^1L \rightarrow {}^1Ru$ energy-transfer processes, a far too large electronic coupling term $H = 105.6\ cm^{-1}$ for the former and $H = 27.69\ cm^{-1}$ for the latter (Table 3) would be necessary. Clearly this would not be consistent with the observed weak interaction between the truxene donor and the metal-based acceptor. Thus, in view of the many simplifications introduced into these calculations and of the limits of the Förster theory in describing closely spaced chromophores with a large conjugation system,[33,34] the predicted energy-transfer-rate constants can be considered to be in acceptable agreement with the experimental findings, as they reproduce both the order of magnitude and the relative reactivity scale. Furthermore, the electronic-coupling constants predicted for a Dexter-type mechanism are inconsistent with the spectroscopically observed weak electronic interaction between the partners. This suggests that the dipole–dipole interaction mechanism is largely predominant for both $^1L \rightarrow {}^1Os$ and $^1L \rightarrow {}^1Ru$ energy-transfer steps within the **RuL^{1}Os** complex, whereas the through-bond-mediated double-electron-exchange contribution to the overall energy-transfer process is expected to be negligible.

The case of the $^3Ru \rightarrow {}^3Os$ transfer process is different. On the basis of the parameters calculated with the available experimental spectroscopic properties of **RuL^1** and **OsL^1** complexes for the Förster-type mechanism, an intermetal separation $d = 10.1$ Å would be required to be $k_F = k_{EnT}$. This distance is significantly shorter then that assumed on the basis of molecular modelling of the **RuOsL^1** dyad, ranging from 21.9 to 25.3 Å depending on the considered configuration (Figure 8). On the other hand, a $J_D = 1.8 \times 10^{-4}$ cm is calculated for a double-electron-exchange mechanism (Dexter-type), which would require a small electronic-coupling term $H = 1.44\ cm^{-1}$, typical of through-bond interaction in condensed aromatic systems,[35] to account for $k_D = k_{EnT}$. Therefore, for the triplet–triplet energy transfer $^3Ru \rightarrow {}^3Os$ step the Dexter-type mechanism prevails over that of dipole–dipole interaction, even if the interchromophoric distance between donor and acceptor is larger than in the $^1L \rightarrow {}^1Os$ and $^1L \rightarrow {}^1Ru$ energy-transfer steps seen above. In fact, when donor and acceptor components are connected through a conjugated bridging ligand, then long-range electronic coupling may occur through an indirect super-exchange process mediated by the orbital of the bridging ligand.[16]

Conclusion

The ligand **L^1**, a truxene scaffold di-substituted with ethynylbipyridine pendant arms, obtained through a Pd^0-promoted statistical cross-coupling reaction, and a series of Ru^{II} and Os^{II} mononuclear and dinuclear complexes have been synthesised. From luminescence measurements, fast energy-transfer processes leading to the final population of Os-based levels have been observed and modelled on the basis of dipole–dipole interaction and double-electron-exchange mechanism.

The energy-transfer cascade in the dyad **RuOsL^1**, initiated upon photoexcitation of the truxene-based electronic levels, proceeds rapidly through i) an efficient $^1L \rightarrow {}^1Os$ direct energy-transfer step followed by ultrafast intersystem crossing to ^3Os or ii) a fast $^1L \rightarrow {}^1Ru$ energy-transfer step and subsequent intersystem crossing to ^3Ru followed by a $^3Ru \rightarrow {}^3Os$ energy-transfer process. For the first $^1L \rightarrow {}^1Os$ and $^1L \rightarrow {}^1Ru$ energy-transfer step the observed process is well modelled on the basis of a dipole–dipole interaction and the contribution to the overall energy-transfer process by the Dexter-type mechanism has proven to be negligible. On the other hand, in the case of $^3Ru \rightarrow {}^3Os$ process the energy transfer is found to be much faster than the maximum possible value predicted for through-space dipole–dipole interaction between the components (Förster mechanism), suggesting the allowance of through-bond mediated Dexter mechanism. Thus, the rigid truxene platform proved to be a suitable platform to promote efficient energy transfer between the Ru^{II} and Os^{II} metal centres, without substantially changing the electronic properties of the individual components.

Experimental Section

Materials: 2,7,12-Triiodo-5,5′-10,10′-15,15′-hexabutyltruxene,[12] [Ru(bpy)$_2$Cl$_2$]·2H$_2$O,[36] [Os(bpy)$_2$Cl$_2$],[37] 5-ethynyl-2,2′-bipyridine,[38] 4-ethynyl-2,2′:6′,2″-terpyridine[38] were prepared according to literature procedures.

General procedure 1 for the counter ion metathesis: The reaction residue obtained after metal complexation was dissolved in the minimum of DMF and added dropwise to a vigorously stirred aqueous solution of KPF_6 (1 g in 10 mL). The resulting precipitate was either filtered off and washed with distilled water, or extracted with dichloromethane, washed with distilled water and then rotary evaporated.

General procedure 2 for the complexation of ruthenium(II): The truxene-2,2′-bipyridine ligand (bpy) was dissolved in a mixture of ethyl alcohol and dichloromethane (v/v 6/1). [Ru(bpy)$_2$Cl$_2$]·2H$_2$O was added and the mixture was refluxed (90 °C) for 3 days. The solvent was then rotary evaporated. The counter ion was exchanged by using general procedure 1 and the residue purified by column chromatography on aluminium oxide, eluting with a mixture of dichloromethane and methyl alcohol, and subsequent recrystallisation in an appropriate solvent mixture.

Synthesis of L^1: 2,7,12-Triiodo-5,5′-10,10′-15,15′-hexabutyltruxene (1.21 g, 1.15 mmol) and 5-ethynyl-2,2′-bipyridine (415 mg, 2.30 mmol) were dissolved in *n*-propylamine (40 mL). Argon was bubbled through the mixture for 30 min, after which [Pd(PPh$_3$)$_4$] (160 mg, 0.14 mmol) was added and the mixture stirred at 60 °C for 18 h. After rotary evaporation of the solvent, the residue was extracted with dichloromethane and washed with water and saturated brine. The organic layer was filtered over hygroscopic cotton wool and evaporated. The target ligand was isolated from remaining starting material, mono-substituted and tri-substituted side products by column chromatography on aluminium oxide eluting with dichloromethane–petroleum ether (v/v 1/9 to 3/7) to give **L^1** as a yellowish-white solid (668 mg; 50 %) after recrystallisation from dichloromethane–ethanol mixture; ^{1}H NMR ((CD$_3$)$_2$CO, 400 MHz): δ = 8.89 (d, 2H, ^4J = 1.5 Hz), 8.72 (d, 2H, ^3J = 4.0 Hz), 8.60–8.52 (m, 6H), 8.33 (d, 1H, ^3J = 8.4 Hz), 8.13 (dd, 2H, ^3J = 8.2 Hz, ^4J = 2.0 Hz), 8.02 (d, 1H, ^4J = 1.8 Hz), 7.97 (td, 2H, ^3J = 7.7 Hz, ^4J = 1.7 Hz), 7.90–7.86 (m, 3H), 7.79–7.76 (m, 2H), 7.47–7.44 (m, 2H), 3.15–3.02 (m, 6H), 2.35–2.20 (m, 6H), 1.05–0.85 (m, 12H), 0.70–0.45 ppm (m, 30H); ^{13}C NMR (CDCl$_3$, 75 MHz): δ = 156.2, 153.9, 153.85, 146.5, 146.3, 145.6, 140.9, 140.8, 139.7, 139.5, 138.2, 138.1, 138.0, 137.3, 135.5, 131.7, 130.3, 126.6, 125.6, 124.8, 124.75, 120.6, 94.5, 92.8, 87.1, 56.1, 55.95, 55.9, 36.8, 36.7, 26.7, 26.6, 23.0, 22.95, 22.9, 14.0, 13.95, 13.9 ppm; EI-MS: *m/e* (nature of the peak, relative intensity): 1161.2 ([*M*]$^+$, 100); elemental analysis (%) calcd for C$_{75}$H$_{77}$IN$_4$: C 77.57, H 6.68, N 4.82; found: C 77.38, H 6.39, N 4.67.

Synthesis of OsL^1: Ligand **L^1** (345 mg, 0.30 mmol) and [Os(bpy)$_2$Cl$_2$] (185 mg, 0.32 mmol) were suspended in ethyl alcohol (20 mL) in a Teflon reactor. The mixture was irradiated with microwaves (1200 W, 180 °C) for 1 h. The solvent was evaporated and counter ion exchanged according general procedure 1. After extraction with dichloromethane, the target compound was isolated from remaining starting material and bimetallic side product by column chromatography on aluminium oxide eluting with dichloromethane–methyl alcohol (v/v 100/0 to 94/6) to afford **OsL^1** as black crystals (227 mg; 40 %) after recrystallisation from dichloromethane–diethyl ether; ^{1}H NMR ((CD$_3$)$_2$CO, 400 MHz): δ = 8.88–8.81 (m, 7H), 8.72 (d, 1H, 4.3 Hz), 8.58–8.51 (4H), 8.33–8.27 (m, 1H), 8.19–7.85 (m, 17H), 7.78–7.73 (m, 1H), 7.6–7.68 (m, 1H), 7.62–7.59 (m, 1H), 7.55–7.45 (m, 6H), 3.13–2.97 (m, 6H), 2.33–2.14 (m, 6H), 1.05–0.82 (m, 12H), 0.66–0.40 ppm (m, 30H); FT-IR (ATR): $\tilde{\nu}$ = 2955, 2927, 2858, 2198 (C≡C), 1065, 1588, 1571, 1460, 1374, 1265, 1066, 833, 760, 726 cm^{-1}; ESI-MS *m/z* (nature of the peak, relative intensity) 1810.4 ([*M*−PF$_6$]$^+$, 100), 832.2 ([*M*−2PF$_6$]$^{2+}$, 30); elemental analysis (%) calcd for C$_{95}$H$_{93}$F$_{12}$IN$_8$OsP$_2$: C 58.40, H 4.80, N 5.73; found: C 58.27, H 4.59, N 5.58.

Synthesis of OsL^2: Complex **OsL^1** (168 mg, 86 μmol) was dissolved in acetonitrile (15 mL) and diisopropylamine (4 mL). Argon was bubbled through the mixture for 30 min, after which [Pd(PPh$_3$)$_4$] (12 mg, 10 μmol) and trimethylsilylacetylene (30 μL, 0.2 mmol) were added and the mixture was stirred at 65 °C for 18 h. The solvent was then rotary evaporated and the counter ion exchanged according general procedure 1. After extraction with dichloromethane, the residue was purified by a quick column chromatography on silica gel eluting with dichloromethane–methyl alcohol (v/v 95/5) to give **OsL^2** as black crystals (157 mg; 95 %) after recrystallisation from dichloromethane–diethyl ether; ^{1}H NMR ((CD$_3$)$_2$CO, 400 MHz): δ = 8.89–8.81 (m, 6H), 8.72 (m, 1H), 8.59–8.45 (m, 5H), 8.19–7.94 (m, 14H), 7.86 (dd, 1H, ^3J = 8.6 Hz, ^4J = 1.6 Hz), 7.79–7.44 (m, 12H), 3.13–2.98 (m, 6H), 2.33–2.15 (m, 6H), 1.03–0.82 (m, 12H), 0.65–0.40 (m, 30H), 0.29 ppm (s, 9H); FT-IR (ATR): ν = 2957, 2926, 2871, 2199 (C≡C), 2152 (C≡C), 1736, 1588, 1572, 1461, 1376, 1248, 1066, 831, 759, 725 cm^{-1}; ESI-MS: *m/z* (nature of the peak, relative intensity): 1779.5 ([*M*−PF$_6$]$^+$, 100), 817.3 ([*M*−2PF$_6$]$^{2+}$, 35); elemental analysis (%) calcd. for C$_{100}$H$_{102}$F$_{12}$N$_8$OsP$_2$Si: C 62.42, H 5.34, N 5.82; found: C 62.59, H 5.08, N 5.62.

Synthesis of RuL^1: Prepared according general procedure 2 from: **L** (20 mg, 0.017 mmol), [Ru(bpy)$_2$Cl$_2$] (8 mg, 0.017 mmol), EtOH (12 mL), CH_2Cl_2 (2 mL); column chromatography on aluminium oxide eluting with dichloromethane–methyl alcohol (v/v 100/0 to 94/6) to afford 16 mg (50 %) of **RuL^1**; ^{1}H NMR ((CD$_3$)$_2$CO, 400 MHz): δ = 8.92–8.82 (m, 7H), 8.75–8.70 (m, 1H), 8.58–8.50 (m, 4H), 8.40–8.21 (m, 9H), 8.15–7.95 (m, 6H), 7.91–7.84 (m, 2H), 7.78–7.73 (m, 1H), 7.69–7.59 (m, 7H), 7.49–7.42 (m, 2H), 3.15–2.95 (m, 6H), 2.33–2.13 (m, 6H), 1.03–0.83 (m, 12H), 0.67–0.40 ppm (m, 30H); FT-IR (ATR): $\tilde{\nu}$ = 2952, 2932, 2860, 2197 (C≡C), 1086, 1594, 1575, 1469, 1375, 1268, 1075, 834, 769, 724 cm^{-1}.

Synthesis of RuOsL^1: Prepared using general procedure 1; from **OsL^1** (50 mg, 25 μmol), [Ru(bpy)$_2$Cl$_2$], ethyl alcohol (30 mL) and dichloromethane (5 mL); column chromatography on aluminium oxide eluting with dichloromethane–methyl alcohol (v/v 98/2 to 95/5) to give **RuOsL^1** as black crystals (53 mg; 79 %) after recrystallisation from dichloromethane–diethyl ether; ^{1}H NMR ((CD$_3$)$_2$CO, 400 MHz): δ = 8.93–8.83 (m, 12H), 8.51 (d, 2H, ^3J = 8.4 Hz), 8.36 (dd, 1H, ^3J = 8.3 Hz, ^4J = 1.9 Hz), 8.28–7.93 (m, 25H), 7.85 (dd, 1H, ^3J = 8.5 Hz, ^4J = 1.7 Hz), 7.69–7.48 (m, 14H), 3.07–2.95 (m, 6H), 2.27–2.13 (m, 6H), 1.00–0.80 (m, 12H), 0.63–0.38 ppm (m, 30H); FT-IR (ATR): ν = 2957, 2928, 2868, 2199 (C≡C), 1604, 1590, 1463, 1446, 1424, 1375, 1266, 1242, 1067, 1027, 828, 759, 727 cm^{-1}; ESI-MS: *m/z* (nature of the peak, relative intensity): 1184.0 ([*M*−2PF$_6$]2^{2+}, 100), 741.4 ([*M*−3PF$_6$]$^{3+}$, 30); elemental analysis (%) calcd for C$_{115}$H$_{109}$F$_{24}$IN$_{12}$OsP$_4$Ru: C 51.98, H 4.13, N 6.33; found: C 52.29, H 4.40, N 6.64.

Synthesis of RuOsL^3: 5-Ethynyl-2,2′-bipyridine (11 mg, 61 μmol) and **RuOsL^1** (125 mg, 47 μmol) were dissolved in a mixture of DMF (12 mL) and diisopropylamine (4 mL). Argon was bubbled through the mixture for 30 min, after what [Pd(PPh$_3$)$_4$] (10 mg, 8.7 μmol) was added and the mixture was stirred at 75 °C for 18 h. The solvent was then rotary evaporated and the counter ion was exchanged according general procedure 1. The residue was extracted with dichloromethane and purified by column chromatography on aluminium oxide eluting with dichloromethane/methyl alcohol (v/v 99/1 to 96/4) to give **RuOsL^3** as a dark solid (71 mg; 56 %) after recrystallisation from dichloromethane–diethyl ether; ^{1}H NMR ((CD$_3$)$_2$CO, 400 MHz): δ = 8.92–8.82 (m, 13H), 8.73–8.71 (m, 1H), 8.58–8.51 (m, 5H), 8.38–8.35 (m, 1H), 8.26–7.94 (m, 25H), 7.86 (d, 1H, ^4J = 1.7 Hz), 7.76 (dd, 1H, ^3J = 8.5 Hz, ^4J = 1.7 Hz), 7.71–7.70 (m, 2H), 7.64–7.45 (m, 13H), 3.12–2.99 (m, 6H), 2.34–2.16 (m, 6H), 1.02–0.83 (m, 12H), 0.66–0.40 ppm (m, 30H); FT-IR (ATR): ν = 2957, 2932, 2856, 2198 (C≡C), 2165 (C≡C), 1618, 1600, 1595, 1460, 1453, 1430, 1370, 1254, 1240, 1102, 1032, 830, 756, 731 cm^{-1}; ESI-MS: *m/z* (nature of the peak, relative intensity): 2563.5 ([*M*−PF$_6$]$^+$, 100), 1211.0 ([*M*−2PF$_6$]$^{2+}$, 45); elemental analysis (%) calcd. for C$_{127}$H$_{116}$F$_{24}$N$_{14}$OsP$_4$Ru: C 56.30, H 4.32, N 7.24; found: C 56.40, H 4.66, N 7.64.

Synthesis of RuOsL^4: Prepared by using the same experimental condition as for **RuOsL^3**; from 4-ethynyl-2,2′:6′,2″-terpyridine (7.2 mg, 28 μmol), **RuOsL^1** (62 mg, 23 μmol), [Pd(PPh$_3$)$_4$] (3 mg, 2.6 μmol), diisopropylamine (3 mL) and acetonitrile (12 mL); column chromatography on aluminium oxide eluting with dichloromethane–methyl alcohol (v/v 95/5) to give **RuOsL^4** as a dark solid (35 mg, 55 %) after recrystallisation from acetone–diethyl ether; ^{1}H NMR ((CD$_3$)$_2$CO, 400 MHz): δ = 8.90–8.74 (m, 16H), 8.67 (s, 2H), 8.59–8.52 (3H), 8.38–8.36 (m, 2H), 8.27–7.94 (m, 26H), 7.86 (dd, 1H, ^3J = 8.2 Hz, ^4J = 1.5 Hz), 7.71–7.70 (m, 2H), 7.64–7.49

(m, 14H), 3.15–2.98 (m, 6H), 2.39–2.15 (m, 6H), 1.03–0.82 (m, 12H), 0.68–0.40 ppm (m, 30H); FT-IR (ATR): ν = 2960, 2927, 2862, 2198 (C≡C), 2168 (C≡C), 1623, 1605, 1599, 1467, 1459, 1433, 1364, 1249, 1236, 1100, 1029, 825, 750, 724 cm^{-1}; ESI-MS: *m/z* (nature of the peak, relative intensity): 2643.0 ($[M-PF_6]^+$, 100), 1248.3 ($[M-2PF_6]^{2+}$, 55), 784.2 ($[M-3PF_6]^{3+}$, 15); elemental analysis (%) calcd for $C_{132}H_{119}F_{24}N_{15}OsP_4Ru$: C 56.89, H 4.30, N 7.54; found: C 56.78, H 4.24, N 7.29.

Optical spectroscopy: Solvents used for photophysical determinations were spectroscopic grade (C. Erba). The absorption spectra of dilute solutions were obtained by using a Perkin–Elmer Lambda 950 UV/vis/NIR spectrophotometer. Molar absorptivity values (ε) were calculated by applying the Lambert–Beer law to low absorbance spectra ($A<1$) of compounds recorded at successive dilutions. Steady-state photoluminescence spectra were measured in right-angle mode by using a Spex Fluorolog II spectrofluorimeter, equipped with a Hamamatsu R928 phototube. The concentration of air-equilibrated sample solutions was adjusted to obtain absorption values $A<0.1$ at the excitation wavelength. Corrected spectra were employed throughout this work by applying to the raw data a correction curve of the wavelength dependent phototube response between λ = 280 and 900 nm obtained by using a calibrated halogen-lamp source. Luminescence quantum efficiencies (ϕ_{em}) in solution were evaluated by using the method of Demas and Crosby by comparing the wavelength integrated intensities (I) with reference to quinine sulfate (ϕ_r = 0.546 in air-equilibrated 1 N H_2SO_4)[25] for the ligand and to $[Ru(bpy)_3]Cl_2$ for the complexes (ϕ_r = 0.028 in air-equilibrated water)[25] as the standard, by using the following Equation (2),[25]

$$\phi_{em} = \frac{A_r n^2 I}{n_r^2 I_r A}\phi_r \tag{2}$$

in which A and n are the absorbance values at the employed excitation wavelength and refractive index of the solvent, respectively. Band maxima and relative luminescence intensities are obtained with uncertainty of 2 nm and 20%, respectively. One cm path length square optical Suprasil Quartz (QS) cuvettes were used for measurements at room temperature of dilute solutions, whereas capillary tubes immersed in liquid nitrogen in a coldfinger quartz Dewar were used for measurements of MeOH/EtOH (1:4) frozen glasses at 77 K. Luminescence lifetimes were measured with an IBH 5000F time-correlated single-photon counting device, by using pulsed NanoLED excitation sources at λ = 331, 465, and 560 nm. Analysis of the luminescence decay profiles against time was accomplished with the Decay Analysis Software DAS6 provided by the manufacturer. Experimental uncertainties in the lifetime determinations are estimated to be 10%.

Energy transfer: For a general energy-transfer process the intramolecular rate constant, can be obtained from Equation (3),[39,40]

$$k_{EnT} = \frac{1}{\tau} - \frac{1}{\tau_0} \tag{3}$$

in which τ is the lifetime of the donor quenched emission and τ_0 is the donor unquenched lifetime. If the quenched donor excited state is too short-lived to be detected, then the same constant can be obtained from the equivalent Equation (4),[39,40]

$$k_{EnT} = \frac{1}{\tau_0}\left(\frac{I_0}{I} - 1\right) \tag{4}$$

in which I_0/I is the luminescence intensity ratio between the unquenched (I_0) and the residual (I) donor emission after the energy-transfer process takes place. The efficiency of the intramolecular energy-transfer process can be evaluated by using Equation (5),

$$\eta_{EnT} = \frac{k_{EnT}}{k_{EnT} + k_{in}} \tag{5}$$

in which $k_{in} = 1/\tau_0$ is the intrinsic deactivation rate constant of the unquenched donor luminophore, and k_{EnT} has been defined before.

For the calculation of the energy-transfer rates based on the Förster and Dexter mechanisms, corrected donor-emission spectra and acceptor-absorption spectra on a wavenumber scale were used. Computations of rate constants and the relevant spectroscopic overlap integrals were performed by using home-developed routines for MATLAB 5.2 (The MathWorks, Inc.). The rate constant for energy transfer according to the Förster (k_F) and Dexter (k_D) mechanism, respectively, were evaluated by employing Equations (6) and (7),

$$k_F = \frac{8.8\times10^{-25}\kappa^2\phi}{n^4\tau d^6}J_F \tag{6}$$

$$k_D = \frac{4\pi^2 H^2}{h}J_D \tag{7}$$

in which $\kappa^2 = 2/3$ is the statistical orientation factor, ϕ is the photoluminescence quantum yield of the donor, n the refractive index of the solvent, τ the excited state lifetime of the donor in ns, d the donor–acceptor distance, taken to be the metal–metal separation calculated from molecular modelling, H is the electronic coupling term, and h is Planck's constant. The spectral overlap integrals J_F and J_D were calculated from the emission spectrum of the donor $D(\bar{\nu})$, and the acceptor absorption spectrum in molar absorptivity units $A(\bar{\nu})$, by using Equations (8) and (9):

$$J_F = \frac{\int D(\bar{\nu})A(\bar{\nu})\bar{\nu}^{-4}d\bar{\nu}}{\int D(\bar{\nu})d\bar{\nu}} \tag{8}$$

$$J_D = \frac{\int D(\bar{\nu})A(\bar{\nu})d\bar{\nu}}{\int D(\bar{\nu})d\bar{\nu}\ \int A(\bar{\nu})d\bar{\nu}} \tag{9}$$

Molecular modelling: Optimised and fixed ground state geometries in vacuo for the complex **RuOsL^1** were obtained by using the PM6[41] semi-empirical quantum mechanical method with built-in parameters, as implemented in the MOPAC2009[42] for Windows package, using the HyperChem[43] GUI. An eigenvector following routine was used as the geometry optimisation method, with a termination condition set by the GNORM = 0.0 and DDMIN = 0.0 parameters.

Acknowledgements

Funding from CNR of Italy (project no. PM.P04.010, "MACOL"), MIUR (FIRB project no. RBIP0642YL, "LUCI"; FIRB project RBIP0642YL, "NODIS"), partial financial support from the French CNRS and University of Strasbourg are acknowledged. S.D. acknowledges the Ministère de la Recherche et de l'Education Nationale for a MRT fellowship. We also thank Johnson Matthey PLC for a loan of precious metal salts.

[1] A. Harriman, R. Ziessel, *Chem. Commun.* **1996**, 1707–1716.
[2] A. Harriman, R. Ziessel in *Carbon-Rich Compounds* (Eds.: M. M. Haley, R. R. Tykwinski), Wiley-VCH, Weinheim, **2006**, pp. 26–89.
[3] B. Gómez-Lor, O. de Frutos, P. A. Ceballos, T. Granier, A. M. Echavarren, *Eur. J. Org. Chem.* **2001**, 2107–2114.
[4] M. H. V. Werts, S. Gmouh, O. Mongin, T. Pons, M. Blanchard-Desce, *J. Am. Chem. Soc.* **2004**, *126*, 16294–16295.
[5] D. Sandstroem, M. Nygren, H. Zimmermann, A. Maliniak, *J. Phys. Chem.* **1995**, *99*, 6661–6669.
[6] T. S. Perova, J. K. Vij, *Adv. Mater.* **1995**, *7*, 919–922.
[7] B. Gómez-Lor, E. Gonzalez-Cantalapiedra, M. Ruiz, S. de Frutos, D. J. Cardenas, A. Santos, A. M. Echavarren, *Chem. Eur. J.* **2004**, *10*, 2601–2608.
[8] C. Moberg, *Angew. Chem.* **1998**, *110*, 260–281 ; *Angew. Chem. Int. Ed.* **1998**, *37*, 248–268.
[9] J. Pei, J. L. Wang, X. Y. Cao, X. H. Zhou, W. B. Zhang, *J. Am. Chem. Soc.* **2003**, *125*, 9944–9945.

[10] M. S. Yuan, Z. Q. Liu, Q. Fang, *J. Org. Chem.* **2007**, *72*, 7915–7922.
[11] S. C. Yuan, H. B. Chen, Y. Zhang, J. Pei, *Org. Lett.* **2006**, *8*, 5701–5704.
[12] S. Diring, R. Ziessel, *Tetrahedron Lett.* **2009**, *50*, 1203–1208.
[13] V. Balzani, A. Credi, M. Venturi, *Molecular Devices and Machines: Concepts and Perspectives for the Nanoworld*, 2nd ed., Wiley, Weinheim, **2008**.
[14] V. Balzani, F. Scandola, *Supramolecular Photochemistry*, Ellis Horwood, Chichester, **1991**.
[15] F. Scandola, M. T. Indelli, C. Chiorboli, C. A. Bignozzi in *Photoinduced Electron Transfer II, Vol. 158* (Eds.: J. Mattay), Springer, Berlin, **1990**, pp. 73–149.
[16] C. Chiorboli, M. T. Indelli, F. Scandola in *Molecular Wires and Electronics, Vol. 257* (Eds.: L. De Cola), Springer, Berlin, **2005**, pp. 63–102.
[17] S. M. Aly, C. L. Ho, D. Fortin, W. Y. Wong, A. S. Abd-El-Aziz, P. D. Harvey, *Chem. Eur. J.* **2008**, *14*, 8341–8352.
[18] S. M. Aly, C. L. Ho, W. Y. Wong, D. Fortin, P. D. Harvey, *Macromolecules* **2009**, *42*, 6902–6916.
[19] B. Ventura, A. Barbieri, F. Barigelletti, J. B. Seneclauze, P. Retailleau, R. Ziessel, *Inorg. Chem.* **2008**, *47*, 7048–7058.
[20] E. M. Pérez, M. Sierra, L. Sanchez, M. R. Torres, R. Viruela, P. M. Viruela, E. Ortí, N. Martin, *Angew. Chem.* **2007**, *119*, 1879–1883; *Angew. Chem. Int. Ed.* **2007**, *46*, 1847–1851.
[21] M. Moreno Oliva, J. Casado, J. T. L. Navarrete, R. Berridge, P. J. Skabara, A. L. Kanibolotsky, I. F. Perepichka, *J. Phys. Chem. B* **2007**, *111*, 4026–4035.
[22] X. Y. Cao, W. Zhang, H. Zi, J. Pei, *Org. Lett.* **2004**, *6*, 4845–4848.
[23] S. Campagna, F. Puntoriero, F. Nastasi, G. Bergamini, V. Balzani in *Photochemistry and Photophysics of Coordination Compounds I, Vol. 280* (Eds.: V. Balzani, S. Campagna), Springer, Berlin, **2007**, pp. 117–214.
[24] D. Kumaresan, K. Shankar, S. Vaidya, R. H. Schmehl in *Photochemistry and Photophysics of Coordination Compounds II, Vol. 281* (Eds.; V. Balzani, S. Campagna), Springer, Berlin, **2007**, pp. 101–142.
[25] M. Montalti, A. Credi, L. Prodi, M. T. Gandolfi, *Handbook of Photochemistry*, 3rd ed., Taylor & Francis, Boca Raton, **2006**.
[26] M. S. Yuan, Q. Fang, Z. Q. Liu, J. P. Guo, H. Y. Chen, W. T. Yu, G. Xue, D. S. Liu, *J. Org. Chem.* **2006**, *71*, 7858–7861.
[27] S. Diring, F. Puntoriero, F. Nastasi, S. Campagna, R. Ziessel, *J. Am. Chem. Soc.* **2009**, *131*, 6108–6110.
[28] C. Chiorboli, C. A. Bignozzi, F. Scandola, E. Ishow, A. Gourdon, J. P. Launay, *Inorg. Chem.* **1999**, *38*, 2402–2410.
[29] G. Orlandi, S. Monti, F. Barigelletti, V. Balzani, *Chem. Phys.* **1980**, *52*, 313–319.
[30] T. Förster, *Discuss. Faraday Soc.* **1959**, *27*, 7–17.
[31] D. L. Dexter, *J. Chem. Phys.* **1952**, *20*, 836–850.
[32] T. Lazarides, A. Barbieri, C. Sabatini, F. Barigelletti, H. Adams, M. D. Ward, *Inorg. Chim. Acta* **2007**, *360*, 814–824.
[33] K. F. Wong, B. Bagchi, P. J. Rossky, *J. Phys. Chem. A* **2004**, *108*, 5752–5763.
[34] L. Flamigni, A. M. Talarico, B. Ventura, R. Rein, N. Solladie, *Chem. Eur. J.* **2006**, *12*, 701–712.
[35] L. Flamigni, A. M. Talarico, F. Barigelletti, M. R. Johnston, *Photochem. Photobiol. Sci.* **2002**, *1*, 190–197.
[36] B. P. Sullivan, D. J. Salmon, T. J. Meyer, *Inorg. Chem.* **1978**, *17*, 3334–3341.
[37] D. A. Buckingham, F. P. Dwyer, H. A. Goodwin, A. M. Sargeson, *Aust. J. Chem.* **1964**, *17*, 325–336.
[38] V. Grosshenny, F. M. Romero, R. Ziessel, *J. Org. Chem.* **1997**, *62*, 1491–1500.
[39] J. L. Sessler, J. Jayawickramarajah, M. Sathiosatham in *Encyclopedia of Supramolecular Chemistry, Vol. 1* (Eds.: J. L. Atwood, J. W. Steed), CRC Press, Boca Raton, **2004**, pp. 535–545.
[40] F. Barigelletti, L. Flamigni, *Chem. Soc. Rev.* **2000**, *29*, 1–12.
[41] J. J. P. Stewart, *J. Mol. Model.* **2007**, *13*, 1173–1213.
[42] MOPAC2009, J. P. Stewart, Stewart Computational Chemistry, Colorado Springs, CO, http://OpenMOPAC.net, **2008**.
[43] HyperChem Professional 8.08, Hypercube, Inc., 1115 NW 4th Street, Gainesville, Florida 32601.

Received: December 2, 2009
Revised: April 6, 2010
Published online: June 25, 2010

